

UC Berkeley

UC Berkeley Previously Published Works

Title

Strain-Driven Mixed-Phase Domain Architectures and Topological Transitions in $\text{Pb}_{1-x}\text{Sr}_x\text{TiO}_3$ Thin Films

Permalink

<https://escholarship.org/uc/item/81n940ms>

Journal

Advanced Materials, 34(37)

ISSN

0935-9648

Authors

Kavle, Pravin
Zorn, Jacob A
Dasgupta, Arvind
[et al.](#)

Publication Date

2022-09-01

DOI

10.1002/adma.202203469

Copyright Information

This work is made available under the terms of a Creative Commons Attribution-NonCommercial-NoDerivatives License, available at <https://creativecommons.org/licenses/by-nc-nd/4.0/>

Peer reviewed

Strain-Driven Mixed-Phase Domain Architectures and Topological Transitions in $\text{Pb}_{1-x}\text{Sr}_x\text{TiO}_3$ Thin Films

Pravin Kavle, Jacob A. Zorn, Arvind Dasgupta, Bo Wang, Maya Ramesh, Long-Qing Chen, and Lane W. Martin*

The potential for creating hierarchical domain structures, or mixtures of energetically degenerate phases with distinct patterns that can be modified continually, in ferroelectric thin films offers a pathway to control their mesoscale structure beyond lattice-mismatch strain with a substrate. Here, it is demonstrated that varying the strontium content provides deterministic strain-driven control of hierarchical domain structures in $\text{Pb}_{1-x}\text{Sr}_x\text{TiO}_3$ solid-solution thin films wherein two types, c/a and a_1/a_2 , of nanodomains can coexist. Combining phase-field simulations, epitaxial thin-film growth, detailed structural, domain, and physical-property characterization, it is observed that the system undergoes a gradual transformation (with increasing strontium content) from droplet-like a_1/a_2 domains in a c/a domain matrix, to a connected-labyrinth geometry of c/a domains, to a disconnected labyrinth structure of the same, and, finally, to droplet-like c/a domains in an a_1/a_2 domain matrix. A relationship between the different mixed-phase modulation patterns and its topological nature is established. Annealing the connected-labyrinth structure leads to domain coarsening forming distinctive regions of parallel c/a and a_1/a_2 domain stripes, offering additional design flexibility. Finally, it is found that the connected-labyrinth domain patterns exhibit the highest dielectric permittivity.

(or “bubbles”). Depending on the system, the characteristic length, or period, of these patterns can vary from a few nanometers (as in directed self-assembly of block copolymers in nanolithography)^[4] to a few microns (as in ripple patterns of alternating superconducting and normal regions in type-I superconductors)^[7] to centimeters (as in convective roll patterns in CO_2 gas undergoing a Rayleigh–Benard instability).^[8] It is the presence of multiple competing interaction forces that gives rise to such spatial inhomogeneities in otherwise uniform ground states. Such modulations can also arise in other order parameters, such as magnetization in films of rare-earth garnets and polarization in ferroelectric films. For example, in thin plates of barium scandium ferrite, application of a magnetic field has been shown to transform the stripe domain state into a periodic array of magnetic bubbles/skyrmions due to the interaction between the long-range magnetodi-

polar force, Dzyaloshinskii–Moriya interaction, and exchange interactions.^[9]


Ferroelectric materials also provide a rich design space for tuning material structure and properties by changing mechanical and electrical boundary conditions. For example, interesting modulations of polarization including polarization vortices,^[10] skyrmions,^[11] and merons^[12] can be observed as one manipulates the energy balance with the boundary conditions. More generally, when grown as films on an appropriate crystalline substrate, ferroelectric materials can accommodate lattice-mismatch stress by forming various patterns of ferroelastic domains.^[13] In the case of a tetragonal ferroelectric such as PbTiO_3 grown on REScO_3 substrates (where $\text{RE} = \text{Dy, Gd, Tb, Sc, Nd}$),^[14] different types of 90° domain configurations form, either so-called c/a (wherein the polar axis alternates from being aligned along the out-of-plane and in-plane directions from domain to domain) or a_1/a_2 (wherein the polar axis is always aligned in the plane of the film, but alternates between being aligned along the $[100]$ or $[010]$) domains can be achieved depending on the strain imposed by the substrate.^[15] Furthermore, these domain structures, when controlled to have similar energies, can produce coexisting mixed-phase polarization structures.^[16] Such coexisting structures have been shown to exhibit facile interconversion between polarization states upon application of mechanical^[17] and electrical^[18] stimuli.

1. Introduction

A diverse set of material classes, ranging from liquid crystals^[1] to polymers^[2–4] to metallic alloys^[5] to ferroic materials^[6] display self-assembled patterns and textures of domains. Formation of these patterns can be viewed as a manifestation of modulated phases. Despite the wide range of materials noted here and their widely varying microscopic structural details and interaction types and strengths, there are certain patterns and textures universally observed in materials, including stripes and droplets

P. Kavle, A. Dasgupta, M. Ramesh, L. W. Martin
Department of Materials Science and Engineering
University of California
Berkeley and Materials Sciences Division
Lawrence Berkeley National Laboratory
Berkeley, CA 94720, USA
E-mail: lwmartin@berkeley.edu

J. A. Zorn, B. Wang, L.-Q. Chen
Department of Materials Science and Engineering
The Pennsylvania State University
University Park, PA 16802, USA

 The ORCID identification number(s) for the author(s) of this article can be found under <https://doi.org/10.1002/adma.202203469>.

DOI: 10.1002/adma.202203469

Besides substrate-induced strain control of domains, compositional control of systems has also been used to realize intricate domain modulations. For example, in single crystals of the $(1-x)\text{BiFeO}_3-(x)\text{PbTiO}_3$ system, researchers have shown a complex hierarchical structure of alternating a - a and a - c domain bands with $x = 0.2$ and stripe-type 109° twin domains with $x = 0.6$.^[19] In compositionally graded $\text{PbZr}_{1-x}\text{Ti}_x\text{O}_3$ heterostructures, researchers have demonstrated the effectiveness of chemistry-driven strain gradients in stabilizing highly susceptible needle-like ferroelastic domains producing a locally enhanced piezoresponse.^[20] Finally, other similar chemistry-controlled ferroelectric heterostructures have shown rich property modulation such as unique hysteresis response,^[21] temperature-stable dielectric permittivity,^[22] and enhanced pyroelectric properties.^[23]

Not only can such phase competition lead to the creation of different kinds of hierarchical domain patterns wherein the constituent phases exist in specific ratios (as dictated by the boundary conditions), but these mixed-phase structures can evolve via different pathways that exhibit similarities to topological processes observed in porous media^[24] and polymers.^[25] Such topologically non-trivial phases in ferroelectric domains,^[26] as in labyrinth and bubble domains in $\text{PbZr}_{0.2}\text{Ti}_{0.8}\text{O}_3$, have recently been shown experimentally and controlled via temperature,^[27] electric field,^[28] mechanical stress,^[29] and/or electrical boundary conditions.^[30] This begs the question if similar topologically distinct phases can be readily tuned in thin films and what the implications of such control of hierarchical, mixed-phase domain structure means for property evolution?

Here, moving beyond simple lattice-mismatch strain with different substrates, we demonstrate that chemistry, namely strontium content in $\text{Pb}_{1-x}\text{Sr}_x\text{TiO}_3$ solid solutions, is a powerful approach to attain deterministic control of hierarchical-domain structures. To do this we combine phase-field simulations, epitaxial thin-film growth, and detailed structural, domain, and physical-property characterization to explore $\text{Pb}_{1-x}\text{Sr}_x\text{TiO}_3$ ($x = 0-0.3$) films grown on DyScO_3 (110) substrates where it is possible to produce continually tunable hierarchical, mixed-phase domain structures wherein c/a and a_1/a_2 nanodomains coexist. Chemical alloying allows for more precise control of the system than using different substrates and, thus, allows for the production of mixed-phase domain structures that exhibit a gradual transformation of the domain morphology from (with increasing strontium content) small isolated a_1/a_2 domains in a c/a domain matrix (henceforth called droplet-like using the language of the field),^[31] to connected-labyrinth c/a domains, to a disconnected labyrinth structure of the same, and, finally, to droplet-like c/a domains in an a_1/a_2 domain matrix. This domain evolution is then studied for its topological nature, using lessons from work on porous media.^[24] This analysis provides additional understanding of the phase-separation kinetics^[32] where we explore not only the phase-fraction evolution, but the evolution of domain connectivity which is important in controlling the overall domain structure. Among the topologically unique structures observed, the connected-labyrinth pattern (which exhibits an array of interesting pattern defects) is annealed and we probe the defect-annihilation process that accompanies the conversion of a disordered structure into another topologically distinct structure with aligned domain

stripes of c/a and a_1/a_2 domains. Finally, the implications of this control of the domain architectures for materials properties are tested by measuring the dielectric response wherein it is found that the materials exhibiting connected-labyrinth patterns, which have the greatest normalized domain-boundary perimeter, also exhibit the highest dielectric permittivity and maximum extrinsic contribution to the same. All told, this offers a nuanced approach to the design of domain-structure architectures and access to a broader range of properties than lattice-mismatch strain alone.

2. Results and Discussion

To understand the evolution of phases and domain structures in our multi-dimensional design space, a detailed thermodynamic description (based on a Ginzburg–Landau–Devonshire (GLD) formalism)^[33] of dense polydomain states in $\text{Pb}_{1-x}\text{Sr}_x\text{TiO}_3$ thin films was developed to calculate the phase diagram of $\text{Pb}_{1-x}\text{Sr}_x\text{TiO}_3$ epitaxial thin films as a function of misfit strain, temperature, and chemistry (x) (Experimental Section). Previously, the phase diagram for $\text{Pb}_{1-x}\text{Sr}_x\text{TiO}_3$ films on DyScO_3 (110) substrates was calculated considering only monodomain configurations;^[34] however, such monodomain states are unlikely except in very thin films since domains are expected to form to lower the free energy of the system.^[35] Here, different possible mono- and poly-domain states were considered while comparing the energy levels and stability regions of various thermodynamically stable phases in the misfit strain-temperature phase diagram for various $\text{Pb}_{1-x}\text{Sr}_x\text{TiO}_3$ compositions (from $x = 0-0.5$ at intervals of $x = 0.05$) to generate a 3D phase diagram (Figure 1a). As expected, different strain values stabilize polarizations along different directions and domain structures because of the competition among various energy terms. For large compressive strains, the $\text{Pb}_{1-x}\text{Sr}_x\text{TiO}_3$ system is predicted to be monodomain c (that is, polarization is fully out-of-plane oriented). Under slight tensile strain, one expects c/a domain formation. At large tensile strains, the a_1/a_2 phase is stabilized (that is, polarization is fully in-plane oriented). Individual strain-temperature phase diagrams for $x = 0.00, 0.10, 0.20, 0.30, 0.40,$ and 0.50 are also provided (Figure S1, Supporting Information). While the GLD formalism provides a starting point to understand the expected domain structures, it fails to address regions of potential mixed-phase coexistence as have been observed in related systems.^[16,36] To further explore the potential for mixed-phase coexistence, we performed phase-field simulations (Experimental Section) with a particular focus on intermediate strain states (-0.2% to 1%) wherein a mixed-phase domain architecture was expected (Figure S2, Supporting Information). In this range, strain accommodation is achieved via formation of a mixture of c/a and a_1/a_2 domain structures (shown in yellow, Figure 1a). Formation of this mixed-phase region can be understood as a decomposition of the material into two distinct domain structures with different strain states (specifically the c/a domains have an in-plane strain $\approx 0.1\%$ and the a_1/a_2 domains have an in-plane strain $\approx 2\%$) in an appropriate proportion so that the overall strain balances to the net in-plane biaxial strain ($\approx 0.2-0.8\%$) imposed from substrate (Figure S3, Supporting Information). In this region, any

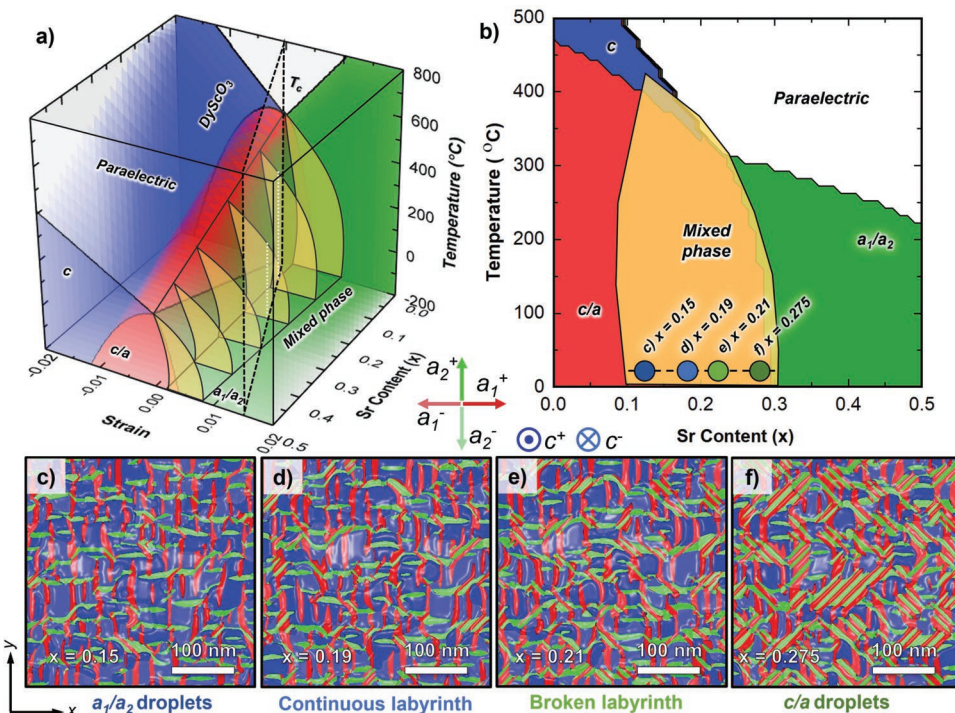


Figure 1. a) Analytical phenomenological modeling-based temperature–strain–strontium content (x) 3D-phase diagram illustrating the stability regimes for paraelectric, c/a , and a_1/a_2 domain structures for $\text{Pb}_{1-x}\text{Sr}_x\text{TiO}_3$ thin films. The mixed-phase domain region where c/a and a_1/a_2 domains coexist is calculated by phase-field simulations and is shown in the yellow color at $x = 0.0, 0.1, 0.2, 0.3, 0.4$ and 0.5 . Strain position of the DyScO_3 (110) is schematically shown as a plane. b) Analytical phenomenological modeling-based temperature–strontium content (x) phase diagram of a $\text{Pb}_{1-x}\text{Sr}_x\text{TiO}_3$ thin film on a DyScO_3 (110) substrate. The mixed-phase region was calculated using phase-field simulations and is shown in yellow. c–f) The mixed-phase region shows a gradual transition in the domain architecture as a function of strontium content (x) such as from small droplets of a_1/a_2 domains inside a c/a domain matrix at $x = 0.15$ (c), to a connected-labyrinth structure of c/a domains at $x = 0.19$ (d), to a disconnected-labyrinth structure at $x = 0.21$ (e), and finally to c/a droplets in an a_1/a_2 matrix at $x = 0.275$ (f).

change in epitaxial strain can be accommodated by changing the relative fractions of c/a and a_1/a_2 domains. At the same time, increasing the strontium content results in a systematic decrease in the Curie temperature because of the decrease in the tetragonality of the $\text{Pb}_{1-x}\text{Sr}_x\text{TiO}_3$ unit cell, also in agreement with previous reports.^[34] All told, this offers an alternative pathway to control the domain architectures. Specifically, we can take a single substrate (here we have chosen growth on DyScO_3 (110) substrates ($a_{\text{pc}} = 3.949 \text{ \AA}$) because it provides an apt starting point with the formation of pure c/a domains with $x = 0$) and propose to vary the strontium composition to provide finer control of the misfit strain and more controllable access to the different hierarchical domain structures (see dashed plane, Figure 1a).

In turn, we can produce a dedicated phase diagram (now in strontium content [x] and temperature space) representing growth on DyScO_3 (110) substrates (Figure 1b) wherein we combine the GLD and phase-field simulations. As expected, starting with small strontium content ($x \lesssim 0.1$) we expect c/a domain structures and then, upon increasing the strontium content, we will first pass through a mixed-phase regime ($0.1 \lesssim x \lesssim 0.3$) before finally entering the a_1/a_2 regime ($x \gtrsim 0.3$). Upon closer inspection, at room temperature and going from lower to higher strontium content, the mixed-phase regime undergoes a gradual transition (Figure S4, Supporting Information). At $x = 0.15$ the system exhibits small droplets of a_1/a_2 domains

inside a c/a -domain matrix (Figure 1c). As the strontium content increases, corresponding to a decrease in the pseudocubic lattice parameter of the $\text{Pb}_{1-x}\text{Sr}_x\text{TiO}_3$ and thus more tensile strain, more in-plane-oriented domains appear resulting in the formation of a connected-labyrinth structure of c/a domains at $x = 0.19$ (Figure 1d) and a disconnected-labyrinth structure at $x = 0.21$ (Figure 1e). Finally, as the strontium content increases further, for example to $x = 0.275$, a_1/a_2 domains grow at the expense of the c/a domain regions forming c/a droplets in an a_1/a_2 matrix (Figure 1f). Previously, similar mixed-phase domain architectures were observed for PbTiO_3 thin film grown on GdScO_3 (110) substrates,^[16] but there was no demonstration of further modulation. Only if the strain can be tuned continuously, as can be done herein with the variable strontium content with one fixed substrate, can one access the phase-field predicted mixed-phase architectures and/or properties which occur only for a narrow range of strain values and with a fine step size of the compositional variation.

To test our predictions, we synthesized a composition series of 100 nm-thick $\text{Pb}_{1-x}\text{Sr}_x\text{TiO}_3$ thin films with $x = 0.00, 0.06, 0.17, 0.20, 0.23, 0.25, 0.27$, and 0.30 on DyScO_3 (110) substrates via pulsed-laser deposition (Experimental Section). Following the growth, detailed structural studies were completed via X-ray diffraction (Figure S5, Supporting Information and Experimental Section) to probe the evolution of the crystal structure (Figure 2a) of the $\text{Pb}_{1-x}\text{Sr}_x\text{TiO}_3$ thin films. High-quality, fully

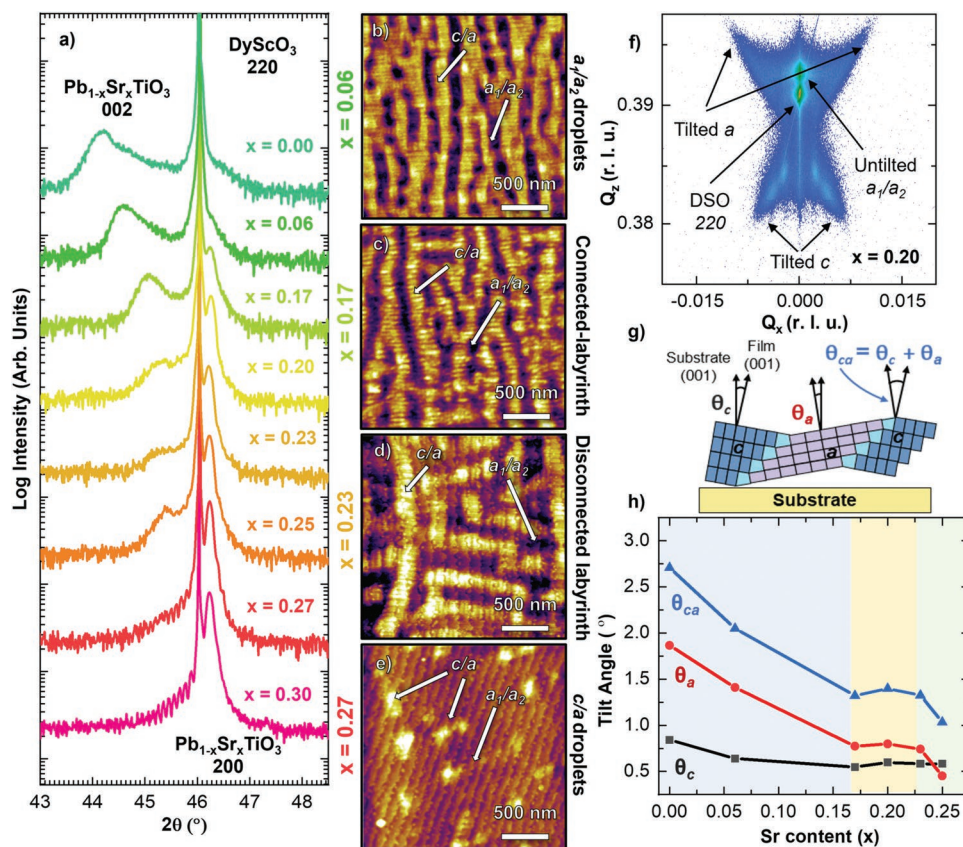


Figure 2. a) θ - 2θ X-ray diffraction scans for 100 nm-thick $\text{Pb}_{1-x}\text{Sr}_x\text{TiO}_3$ thin films (with, from top to bottom, $x = 0, 0.06, 0.17, 0.20, 0.23, 0.25, 0.27$, and 0.30) grown on DyScO_3 (110) substrates. b–e) AFM topography images of the $\text{Pb}_{1-x}\text{Sr}_x\text{TiO}_3$ thin films showing a_1/a_2 droplets in a c/a matrix for $x = 0.06$ heterostructures (b), a connected-labyrinth structure for $x = 0.17$ heterostructures (c), a disconnected-labyrinth structure for $x = 0.23$ heterostructures (d), and c/a droplets in an a_1/a_2 matrix for $x = 0.27$ heterostructures (e). f) RSM about the 220-diffraction peak of the DyScO_3 (110) substrate revealing 002- and 200-diffraction peaks for the $\text{Pb}_{1-x}\text{Sr}_x\text{TiO}_3$ thin films corresponding to the tilted c and tilted/untilted a domain variants, respectively, for an $x = 0.20$ heterostructure. g) Schematic of the domain tilting phenomenon observed in the c/a domain stripes with characteristic angles defined. h) Measured tilt angles for the c and a domains and the net tilt angle between them as a function of film composition.

epitaxial solid-solution films were obtained for all compositions studied herein. The $\text{Pb}_{1-x}\text{Sr}_x\text{TiO}_3$ ($x = 0$ – 0.3) 002-diffraction peaks, in all cases, appear to shift to higher θ - 2θ values with increasing strontium content (corresponding to a reduction of the out-of-plane lattice parameter) along with the appearance of the 200-diffraction peak. This is consistent with what is expected for isovalent substitution of a smaller-sized Sr^{2+} cation (144 pm) at the Pb^{2+} (149 pm) site. Coexistence of both the 002- and 200-diffraction peaks observed in the composition range $x = 0.06$ – 0.27 points to the formation of mixed-phase domain architectures. At $x = 0.30$, only a single (strong) peak corresponding to the 200-diffraction peak is observed, indicating single-phase a_1/a_2 domains.

Examination of the surface topography using atomic force microscopy (AFM, Figures S6 and S7, Supporting Information and Experimental Section) reveals systematic evolution of the hierarchical-domain structures^[16] (Figure 2b–e) in agreement with both the phase-field simulations and the X-ray diffraction. Two distinct areas are observed in each topography image: the areas with elevated topography (bright in the images) are the c/a -domain regions and the lower-lying regions (dark in the images) are the a_1/a_2 -domain regions.

These hierarchical domain structures show four broad categories of morphology based on the distribution and connectivity of the c/a domains across intermediate strontium compositions ($0.06 \leq x \leq 0.27$). Starting with $x = 0.06$ heterostructures (Figure 2b), a predominantly c/a domain structure with small droplet-shaped a_1/a_2 regions are observed. Upon increasing the strontium content to $x = 0.17$ (Figure 2c), what is called a connected-labyrinth structure of the c/a domains is observed. To accommodate the increased strain induced by the presence of additional strontium, the individual a_1/a_2 droplet regions elongate (and increase in volume fraction) and create a connected labyrinthine pattern of c/a domains. Further increasing the strontium content to $x = 0.25$ results in the formation of a broken-labyrinth structure of the c/a domains (Figure 2d). Instead of reducing the c/a domain stripe width, the structure prefers to break down into smaller length scale c/a domain stripes to accommodate an increased a_1/a_2 domain fraction. Finally, when $x = 0.27$ (Figure 2e), the majority phase is now the a_1/a_2 domain structure with sparsely dispersed c/a domain droplets; essentially an inverse replica of the $x = 0.06$ heterostructures where there were droplets of a_1/a_2 domains in a c/a matrix. Finally, at the composition extremes studied herein,

$x = 0.0$ and 0.3 , the heterostructures show prototypical pure c/a and a_1/a_2 domain patterns, respectively (Figures S6 and S7, Supporting Information).

Further understanding of the hierarchical domain architectures can be obtained by studying different features in X-ray reciprocal space mapping (RSM) studies (Experimental Section). While RSMs for heterostructures of all compositions studied herein are provided (Figure S8, Supporting Information), here, for brevity, we use an RSM about the 220_{O} -diffraction condition of the DyScO_3 substrate for an $x = 0.20$ heterostructure to explain the pertinent features (Figure 2f). The RSM reveals film peaks corresponding to 002-oriented c domains as well as two versions of in-plane polarized a domains: 1) an untilted variant (arising from the classic a_1/a_2 structure) and 2) a tilted variant (arising from the a domains in the c/a structure). The lattice matching between the c and a domains in the c/a domains involves the tilt of the individual c and a domains such that the coherent boundary between them lies on a $\{101\}$. A schematic of such a c/a domain structure (Figure 2g) shows this domain-tilting phenomenon where the tilt angles θ_c and θ_a refer to the tilts of the c and a domains, respectively, relative to the film normal $[001]$ and an a total characteristic angle $\theta_{ca} = \theta_c + \theta_a$ is defined to provide a single metric to describe the structure. These tilt angles are extracted for heterostructures of composition $x = 0.00, 0.06, 0.17, 0.20, 0.23$, and 0.25 (Figure 2h) and it is found that as the strontium content increases, the tilt angles decrease continuously for lower strontium contents ($0 < x < 0.17$) before leveling off at intermediate strontium contents ($0.17 < x < 0.23$; where domains exist in connected- and broken-labyrinth patterns) and then ultimately decreasing further as the strontium content increases further ($x > 0.23$). The angle θ_{ca} depends on the ratio of the long and short unit cell lengths.^[37] Thus, a net decrease in θ_{ca} can be explained by the reduction in out-of-plane lattice parameter that corresponds with increasing strontium content (Figure 2a). Consequently, this can also provide an effective tool to tune tilt angle θ_{ca} in a controlled manner which could impact both the dielectric response and polarization switching processes.^[38]

One interesting observation is that, upon increasing the strontium content, instead of just enlarging the isolated a_1/a_2 droplets observed at $x = 0.06$, the system self-assembles into a new structure (the connected-labyrinth pattern of c/a domains) at $x = 0.17$. Such changes in the domain structure are similar to effects observed in polymer blends^[39] and porous media^[40] where the topology of the structures changes from “bubbles” to “cylinders” to “bicontinuous networks” to “lamellar structures” upon changing the relative concentration of the two constituents and/or temperature.^[41] In these cases, as is seen herein for the ferroelectric domain structures, the result is that not only does the phase fraction of the secondary phase change, but also how that phase is arranged within the primary phase. In turn, taking lessons from these other fields of study, we have applied analysis approaches developed therein^[42–44] to the domain structures observed herein. In particular, we translate ideas of topology (a branch of mathematics that offers a means to characterize the shape of data objects)^[44] including the so-called Euler characteristic (EC) which is a topologically invariant number that describes a topological space’s shape or structure regardless of the way it is bent or stretch without breaking,^[45] to explore these domain structures. The EC has

seen limited applications in engineering, but has been used to describe porous media^[46] and fluids within them,^[24] where the topological characteristics of the porous media calculated by EC, together with the pore size distribution, provide a good projection of the effective hydraulic properties and transport.^[47] Recently, however, similar topological characterization has been applied to ferroelectrics to identify the transition from a labyrinth pattern (formed via a suspected spinodal decomposition) to a bubble-domain pattern (formed via nucleation) induced via applied electric field in $\text{PbZr}_{0.2}\text{Ti}_{0.8}\text{O}_3$ by effectively using the phase fraction and percolation threshold of the minority phase.^[26] In that regard, EC can provide a robust descriptor of phase distribution and connectivity without being affected by the size and shapes of various domains, information which is missing in many statistical descriptors.^[42]

Again, here it was observed that upon increasing the strontium content in the $\text{Pb}_{1-x}\text{Sr}_x\text{TiO}_3$ thin films, the mixed-phase domain structure undergoes a gradual transformation as observed via phase-field simulations (Figure 1c–f) and AFM topography (Figure 2b–e). To show the similarity in the experimental and simulation results and support our analysis, we provide three types of information for a selection of compositions studied herein (i.e., experimental $x = 0.06, 0.17, 0.23$, and 0.27 ; Figures 3a–d, respectively): 1) an AFM topography image, 2) a phase-field simulation (scaled to a similar length scale as the AFM image), and 3) a binarized image of the corresponding AFM and phase-field data wherein the white and black colors correspond to the c/a and a_1/a_2 regions and are used for the subsequent topological analyses (Experimental Section). As expected, the phase-field simulations and experimental data show similar trends in the evolution of the hierarchical-domain structures, albeit with an offset in terms of the chemistry. This difference in chemistry is explained by the fact that the phenomenological thermodynamic potential used in this work may overestimate the stability of the c/a -domain regions as well as provide slight variations of the Curie temperature values for different compositions of strontium.^[48,49] Additionally, there are varying reports on the compositions and temperatures at which the $\text{Pb}_{1-x}\text{Sr}_x\text{TiO}_3$ crystal becomes cubic^[50–52] which also plays a factor in directly translating the chemistries between simulation and experiment. Considering these numerical and experimental constraints, we believe such differences between the two curves are inconsequential to the main conclusions of the present study and the trends of the data and resulting structures are found to be identical.

Focusing now on the binarized images, the EC number χ (Figure S9a, Supporting Information) is calculated as the total number of objects (i.e., the distinct number of c/a -domain regions) minus the total number of holes (i.e., distinct number of a_1/a_2 -domain regions). This simple approach, however, has the challenge that there can be both different total numbers of objects/holes in the various AFM images and the numbers would depend on image size. Thus, to assure the production of comparable numbers, we defined a normalized EC number χ_N , which is defined as the average number of discrete topological features that the morphology supports relative to total number of features as defined as:

$$\chi_N = \frac{(\text{Number of Objects (O)} - \text{Number of Holes (H)})}{(\text{Number of Objects (O)} + \text{Number of Holes (H)})} \quad (1)$$

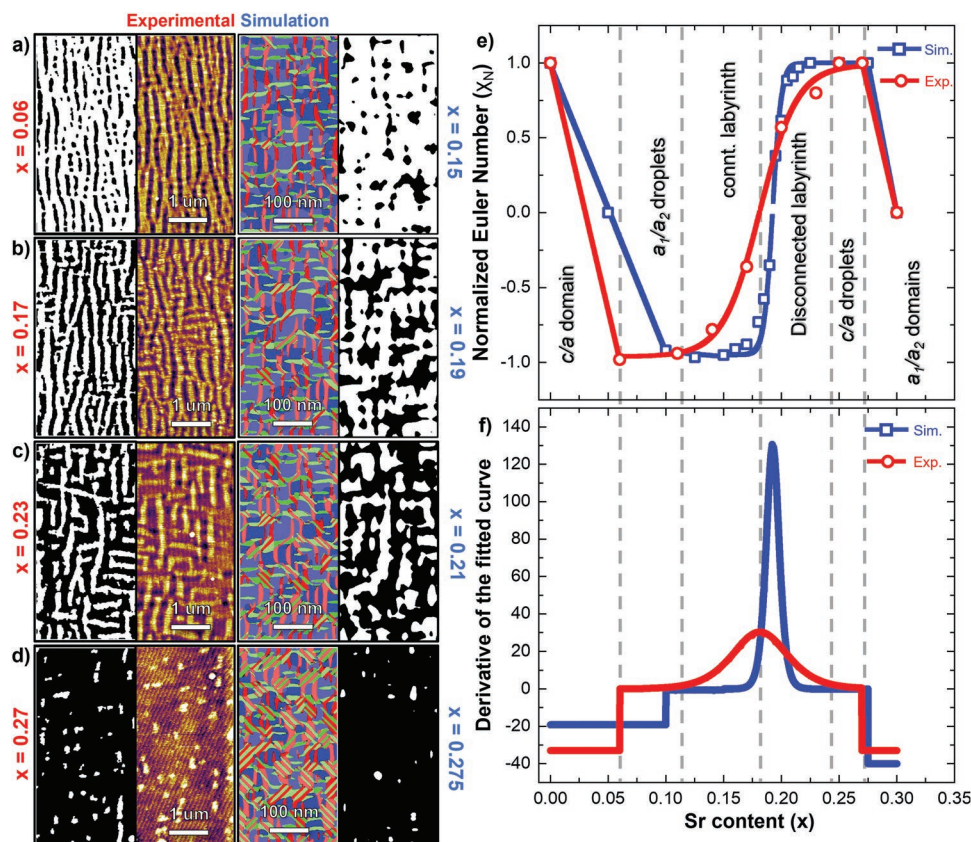


Figure 3. a–d) From left to right, a binarized image used for analysis based on the experimental AFM data, the AFM topography image, the corresponding phase-field simulation, and a binarized image used for analysis based on the phase-field simulation for $\text{Pb}_{1-x}\text{Sr}_x\text{TiO}_3$ thin films with $x = 0.06$ (a), $x = 0.17$ (b), $x = 0.23$ (c), and $x = 0.27$ (d) (experimental x values noted here, but corresponding phase-field x values are noted on the figure). e) Calculated normalized Euler characteristic (χ_N) versus strontium content (x) for the experimental part (red circles) and phase-field generated (blue squares). f) Derivative of the piecewise fitted curve of the normalized Euler characteristic (χ_N) for the experimental and simulated data. Extrema of the derivative of the experimental curve (red line) are used to demarcate various topological regions observed in the $\text{Pb}_{1-x}\text{Sr}_x\text{TiO}_3$ thin films.

This characterization approach is, thus, independent of the domain size, domain numbers, domain-boundary roughness, and shape of the domain-wall patterns (Figure S9b–g, Supporting Information).

The evolution of χ_N (with respect to the c/a -domain structure; Experimental Section and Figures S10 and S11, Supporting Information) was determined for various $\text{Pb}_{1-x}\text{Sr}_x\text{TiO}_3$ thin films (Figure 3e) as a function of strontium content for the microstructure produced by both phase-field simulations (Figures S12 and S13, Supporting Information) and the AFM data. As noted, there is a slight difference between the evolution of χ_N for the phase-field simulation and experimental strontium content values.

As we step through the piecewise fitted curve of χ_N , we find that at a local minimum it has “holes” throughout the area (i.e., a_1/a_2 droplets as in the $x = 0.06$ heterostructures). When it passes through a saddle point, multiple objects are joined to form connected-labyrinth structures of c/a domains (as in the $x = 0.17$ heterostructure). And at a local maximum, we have the majority objects scattered without any holes inside them (as in the c/a droplets in $x = 0.27$ heterostructures). It has been widely observed that the logarithm density of the EC, $\log(|\chi|)$ (i.e., the Euler entropy), shows singular behavior

around a thermodynamic phase transition in theoretical models^[53,54] as well as around the zeros of the EC.^[55–59] This has led to the introduction of topological phase transitions as the loci of such critical points of the EC,^[60] where there is a large component (objects or holes) transition in the neighborhood.^[61] Thus, the location of different topological transitions occurring as the system evolves from pure c/a domains to pure a_1/a_2 domains via the mixed-phase region can be inferred by taking the derivative (Figure 3f) of the piecewise fitted curve of χ_N and the extrema of these derivatives are used to demarcate different characteristic zones, the boundaries between which represent the geometric growth or decay in the domain numbers.^[26] The different regions including: 1) pure c/a domains, 2) a_1/a_2 droplets in a c/a matrix, 3) connected-labyrinth structure of c/a domains, 4) broken-labyrinth structure of c/a domains, 5) c/a droplets in an a_1/a_2 matrix, and 6) pure a_1/a_2 domains can be identified using this method. This approach provides novel insight into the strain-field tuning of domain structures and ferroelectric topological nanostructures and helps open the door for the new field of “topological strain-field engineering”^[62] and “topological defectronics.”^[63,64]

Building from these observations, we focused specifically on the continuous-labyrinth structure which showed

local ordering up to a certain finite length and also exhibited the most types of pattern defects in its as-grown state. Upon annealing, such labyrinth patterns have shown transformation into parallel-stripe patterns in ferroelectrics;^[27] a behavior which is analogous to the inverse-transition phenomenon observed in magnetic films^[65,66] and explained via topological-defect annihilation. In that regard, to study to what extent this potentially metastable continuous-labyrinth morphology is kinetically constrained, we performed a series of annealing experiments (Experimental Section) wherein, briefly, samples were annealed to 270 °C for increasing lengths of time (12–190 h) and then cooled to room temperature where we completed AFM imaging to explore the evolution of the domain structures (Figure S14, Supporting Information) in the same region (Figure 4a). The realignment to the unidirectional stripe domain pattern starts after just a few hours (Figure 4b). The same area, after 190 h of annealing (Figure 4c), shows distinct *c/a*- and *a*₁/*a*₂-domain stripe ordering (along the vertical direction of the images). The macroscopic nature of this ordering is confirmed by RSM studies (Figure S15, Supporting Information). The ordering distance measured from AFM topography (≈400 nm) matches well with the distance calculated from the satellite ordering peaks (≈390 nm) in the RSM studies. It should also be noted that the overall phase fraction of the *c/a* domains and the shared perimeter between the *c/a*- and *a*₁/*a*₂-domain remains constant over successive annealing cycles (Figure S16a, Supporting Information). Also, there are no structural changes in the Pb_{0.83}Sr_{0.17}TiO₃ thin film with increasing annealing time (Figure S16b, Supporting Information). Finally, there is a change in the normalized EC, representing the realignment of connected labyrinth structure to the stripe domains (Figure S16c, Supporting Information).

The phase-field simulations (Figure 4d) show a similar domain stripe reordering phenomenon upon short (Figure 4e) and long (Figure 4f) annealing process. It is seen that at an annealing temperature of 277 °C (550 K), the domain structure consists predominantly of *a*₁/*a*₂ twin structures (Figure S17b, Supporting Information). This agrees with the phase diagrams described earlier (Figure 1b), where the high-temperature phase at intermediate strontium content is close to the mixed-phase and *a*₁/*a*₂ polydomain boundary. Upon cooling, however, *c* domains begin to form and create *c/a* regions that lead to the formation of regularly arranged stripe domains (Figure S17d, Supporting Information). Again, the phase fractions of the *a*₁/*a*₂ and *c/a* regions remain essentially constant throughout the annealing cycles (Figure S17e, Supporting Information). This realignment process also leads to the overall lowering of the energy of the system (Figure S18f, Supporting Information) as the energy difference between the as-grown state and the longest (600 000 timesteps) annealed sample changes by nearly 9%. Evolution of different energy terms (i.e., elastic, electrostatic, bulk Landau energy, and short-range gradient energy; Figure S19a–d, Supporting Information) can also be extracted as a function of annealing time. Untangling of the labyrinthine pattern reduces the short-range gradient energy significantly. This global free energy minimization allows us to visualize the complex reorganization within different types of labyrinthine patterns^[67] as compared to as-grown, glass-like kinetically arrested states.^[68]

This ordering process can be further understood by the analysis of the pattern-defect densities as a function of annealing time. For that, we identified different types of elementary and composite defects during the annealing process. Among these multiple defects, threefold junctions (concave disclinations, Figure 4g) and stripe-endpoints (convex disclinations, Figure 4h) are identified as primary defects, like those previously defined for defects in liquid crystals.^[69] Further, they combine within themselves to form multiple other types of composite defects.^[70] For example, by combining two threefold junctions it is possible to form a saddle defect (i.e., a fourfold defect; Figure 4i) and by combining a threefold junction and stripe endpoint it is possible to produce a handle defect (Figure 4j). Further observation revealed other types of defects, namely isolated stripe segments (Figure 4k), dots (Figure 4l), target skyrmions (Figure 4m),^[71] and dislocation-style (Figure 4n) defects. Examination reveals that the density of type-1 (*D*_{type1}; e.g., fourfold and threefold junctions) and type-2 (*D*_{type2}; e.g., stripe endpoints) defects (Figure S20, Supporting Information), shows a steady decrease as a function of annealing time (Figure 4o). In the early stages of annealing, the majority type-1 defects annihilate. Thus, junctions can be seen as the weak links of the connected-labyrinth structure as they are first to disappear during the annealing process. In the later stages of annealing, the density of type-2 defects also decreases significantly. This reduction in defect densities can be understood as a recombination and annihilation of defects,^[69,72] where, for example, a pair of concave and convex disclinations can combine leading to the unidirectional stripe domain with new periodicity. Such control via annealing over the self-assembly of domain patterns provides an additional knob, beyond conventional domain engineering^[73] and domain-wall-based^[74] methodologies, to manipulate domain structure morphologies.

Thus far we have demonstrated an exacting and extensive pathway to control domain structures in ferroelectrics. This is of particular interest since it is well known that domain structures can greatly impact the evolution of properties (e.g., dielectric,^[75,76] piezoelectric,^[77] and pyroelectric^[23,78]) in ferroelectrics. To study the effect of our ability to continually manipulate the domain structures on the properties, the dielectric constant (ϵ_r) was measured (Experimental Section). To do this, 30 nm SrRuO₃/100 nm Pb_{1-x}Sr_xTiO₃ (*x* = 0.00, 0.06, 0.17, 0.20, and 0.30)/30 nm SrRuO₃/DyScO₃ (110) heterostructures were fabricated into capacitor structures (Experimental Section). First, polarization-electric field hysteresis loops (reported at 10 kHz) were measured and, as anticipated, the largest saturated polarization (*P*_s) values were observed for the *x* = 0.00 heterostructures, while the *x* = 0.30 heterostructures exhibited the lowest (Experimental Section and Figure S21, Supporting Information). As the strontium content is increased, there is a systematic increase in the *a*₁/*a*₂-domain fraction in the mixed-phase domains which manifests as an overall increase in the out-of-plane dielectric response (Figure 5a); as ϵ_r is higher for *a* domains than for the *c* domains in the measured geometry.^[79] With this trend, ϵ_r can be seen reaching a maximum value in the connected-labyrinth (*x* = 0.17) heterostructures, suggesting that additional new domain boundaries are forming between the *c/a* and *a*₁/*a*₂ domains (henceforth referred to as the interdomain boundaries; Figures S22 and S23, Supporting Information)

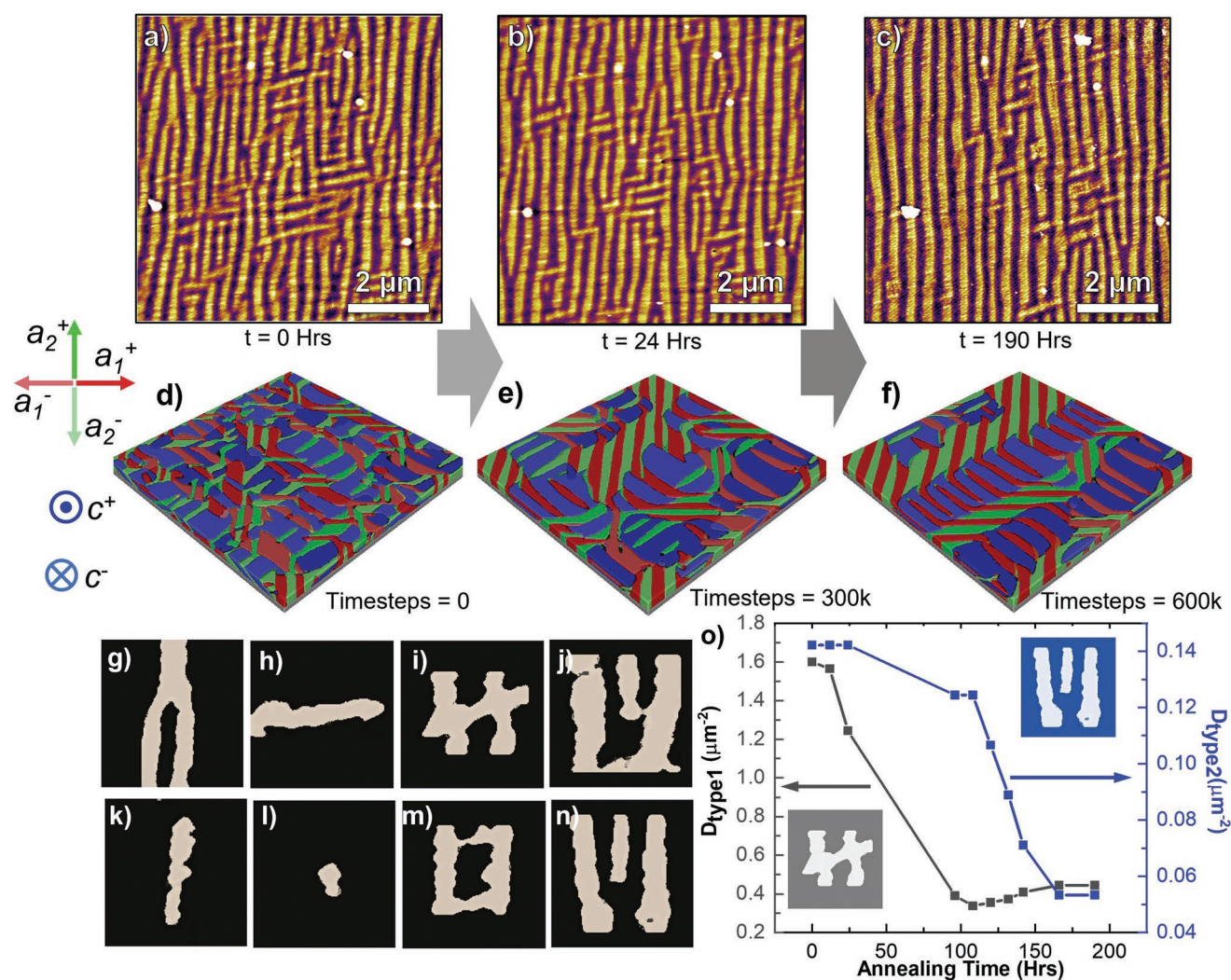


Figure 4. a–c) AFM topography images of 100 nm-thick $\text{Pb}_{0.83}\text{Sr}_{0.17}\text{TiO}_3$ thin films grown on DyScO_3 (110) substrates in the as-grown state (a) and in the same area after annealing at 270°C for 24 h (b) and 190 h (c). d–f) Phase-field simulations showing similar domain alignment phenomenon in the connected-labyrinth structure for the as-grown state (d) and after annealing for 300 000 (e) and 600 000 (f) timesteps. g–n) Various types of defects are observed in the $\text{Pb}_{0.83}\text{Sr}_{0.17}\text{TiO}_3$ thin films such as threefold junctions (g), stripe end-points (h), fourfold junctions (saddle points) (i), handle defects (j), disconnected stripes (k), droplets (l), target skyrmions (m), and dislocations (n). o) The defect densities of three- and four-fold junctions (D_{type1}) and the stripe end-points (D_{type2}) as a function of annealing time. The insets show the dislocation and fourfold defect types.

and potentially affecting the net dielectric response largely by introducing added extrinsic contributions^[75,76] over the regular higher contribution introduced by increasing the overall a_1/a_2 -domain fraction. To understand this potential effect, we extracted the shared perimeter between the c/a and a_1/a_2 domains from the AFM images and then normalized by the area of the majority domain variant to calculate a so-called normalized interdomain perimeter (Figure 5b). This value also reaches its maximum value at $x = 0.17$, the same composition at which ϵ_r is maximized. This indicates a connection between the interdomain boundaries and the dielectric response.

This can be taken one step further since the total contribution to ϵ_r can be divided into multiple sources, including intrinsic (arising from the polarization within the ferroelectric domains) and extrinsic (arising from the movement of domain walls) contributions. To quantify these contributions, the

dielectric permittivity was measured as a function of frequency between 5 and 1000 kHz at different applied background DC electric fields (Experimental Section and Figure S24, Supporting Information). The applied background DC electric field can suppress the extrinsic contributions and allows for quantitative measurement of the intrinsic response.^[80] By fitting the frequency (f) dependence of the permittivity with each applied background DC electric field to the equation $\epsilon = \epsilon_i - \alpha \log f$, the DC biased dependence of the zero-field dielectric constant intercept (ϵ_i) and slope (α) can be calculated. The magnitude of the dielectric constant decreases as the applied background DC electric field is increased from 0 to -420 kV cm^{-1} (shown here, as an example, for an $x = 0$ heterostructure; Figure 5c). ϵ_i is then obtained from a linear logarithmic fit of the dielectric permittivity-frequency data at different applied background DC electric fields. These intercepts are then plotted as a function of

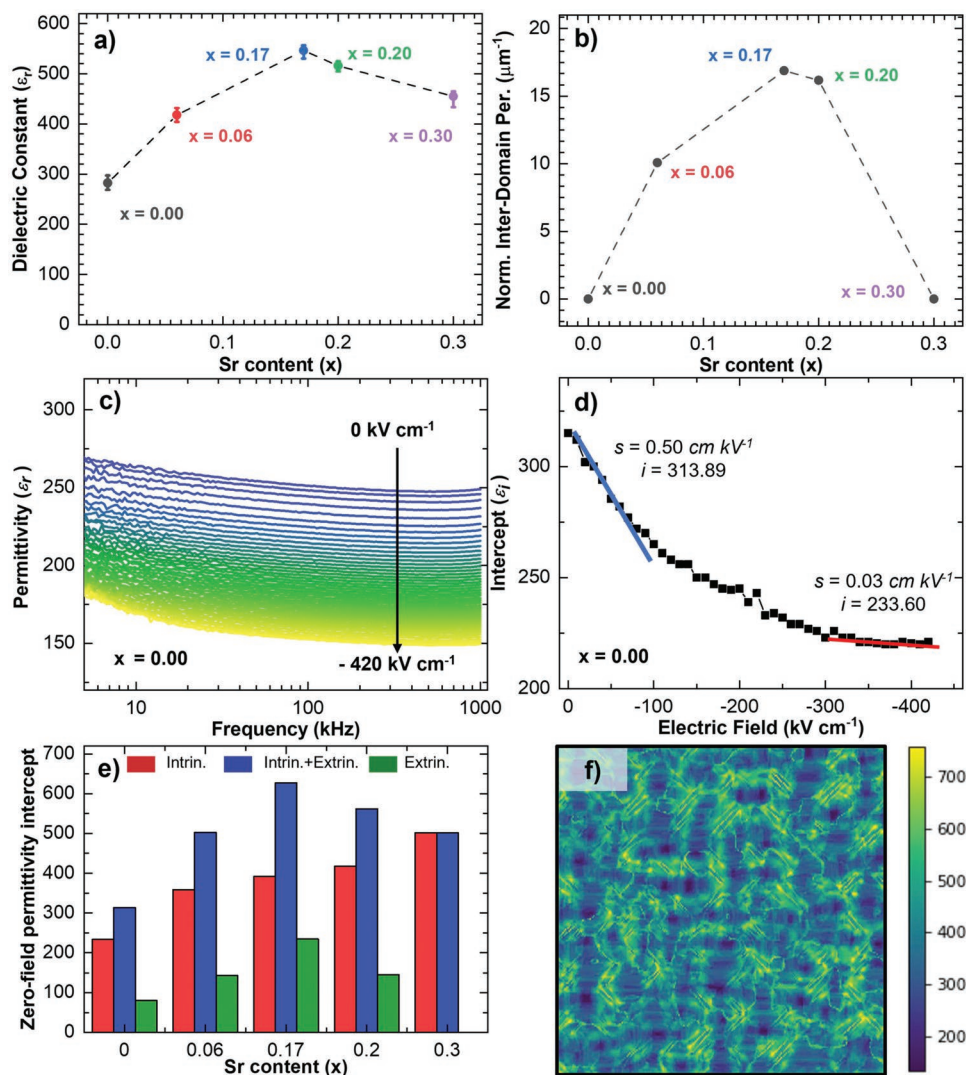


Figure 5. a) Dielectric permittivity (ϵ_r) as a function of strontium content (x). b) Shared perimeter between c/a and a_1/a_2 domains normalized by majority phase as a function of strontium content (x). c) Dielectric permittivity as a function frequency measured at different applied background DC electric fields for $x = 0.00$ heterostructure. d) Intercepts obtained from a linear logarithmic fit of the dielectric permittivity–frequency plot at various applied background DC electric fields are plotted as a function of the applied DC electric fields for $x = 0.00$ heterostructure. e) Zero-field permittivity intercept of Intrinsic-only, combined intrinsic–extrinsic contribution, and the difference between them (extrinsic-only contribution) is plotted as a function of strontium content (x). f) Phase-field simulations for permittivity coefficient (k_{33}) for mixed-phase $\text{Pb}_{1-x}\text{Sr}_x\text{TiO}_3$ thin film with $x = 0.1875$.

applied background DC field to obtain values of the zero-field intercept and slope for two distinct regions (again, shown here for an $x = 0$ heterostructure as an example; Figure 5d). The low-field regime comprises the combined intrinsic and extrinsic contributions (fitted with blue line), and the high-field regime is indicative of the intrinsic response (fitted with red line). Similar analysis was done for other compositions (Figure S24, Supporting Information). As one moves from low to higher strontium content ($0 \leq x \leq 0.3$), while the overall dielectric response (intrinsic and extrinsic contributions) is maximum at $x = 0.17$, the intrinsic contribution is found to increase systematically with strontium content as expected from the increasing a_1/a_2 domain fraction. The maximum value at $x = 0.17$, in turn, arises from the fact that this composition has the largest extrinsic contribution ($\approx 38\%$ of the overall response). This is

in comparison to the $x = 0$ (pure c/a -domain structure) and $x = 0.3$ (pure a_1/a_2 -domain structure) heterostructures where the extrinsic contribution makes up only 26% and 0% of the overall response. The presence of the mixed-phase structures and the interdomain boundaries (as for the $x = 0.06, 0.17$, and 0.2 heterostructures) results in larger extrinsic contributions and higher overall responses.

To further examine the impact of interdomain boundaries on the properties, we performed phase-field simulations and calculated the dielectric constant (k_{33}) for a mixed-phase $\text{Pb}_{0.8125}\text{Sr}_{0.1875}\text{TiO}_3$ thin film (Figure 5f). We can see the enhanced dielectric coefficient (k_{33}) at the interdomain boundaries signifying increased activity. This is qualitatively like what is seen in the experimental work of the $\text{Pb}_{1-x}\text{Sr}_x\text{TiO}_3$ solid solutions for dielectric permittivity (Figure 5a). These results

signify that the distinct topological structures engineered so far in various material systems ranging from polymers^[2,3] to liquid crystals,^[1] can also be engineered in ferroelectric systems to enhance their functional properties.

3. Conclusion

All told, by combining epitaxial thin-film growth and various characterization methods with phase-field simulations, we have systematically investigated the evolution of complex, mixed-phase domain structures in the $\text{Pb}_{1-x}\text{Sr}_x\text{TiO}_3$ system as a function of strontium content. Unlike simple lattice-mismatch strain, the combination of strain, chemistry, and annealing provide for a fine level of control of the domain patterns, phase fractions, domain-wall length, etc. In turn, these structures have been analyzed for their topological nature and using approaches adapted from other fields, we identify a number of topological transitions across these different patterns. Further annealing the connected-labyrinth structures results in defect annihilation and ordering of the system into parallel-stripe domain patterns of c/a and a_1/a_2 domains, thus providing additional control of the system. In turn, this control has an impact on the properties of the films. By measuring the dielectric response for the different domain structures, it is found that the highest dielectric constant and maximum extrinsic contribution to the dielectric response occur when the domains are arranged in the connected-labyrinth structures.

4. Experimental Section

Thermodynamic Approximations: The bulk free energy of a ferroelectric system could be described using GLD theory. Commonly, this energy could be described by a Taylor expansion about the spontaneous polarization, that is,

$$f_{\text{Landau}}(P_i) = \alpha_1(P_1^2 + P_2^2 + P_3^2) + \alpha_{11}(P_1^4 + P_2^4 + P_3^4) + \alpha_{12}(P_1^2P_2^2 + P_1^2P_3^2 + P_2^2P_3^2) + \alpha_{111}(P_1^6 + P_2^6 + P_3^6) + \alpha_{112} \left(\frac{P_1^4(P_2^2 + P_3^2)}{+P_2^4(P_1^2 + P_3^2)} + P_3^4(P_2^2 + P_1^2) \right) + \alpha_{123}P_1^2P_2^2P_3^2 \quad (2)$$

where α_i , α_{ij} , and α_{ijk} were the dielectric stiffness coefficients measured under constant stress boundary conditions and P_i represented the spontaneous polarization (measured in C m^{-2}). It was noted here that the reference frame was the traditional Cartesian coordinate system (i.e., subscript 1 was parallel to the (100), 2 was parallel to the (010), and 3 was parallel to (001)). The elastic energy could be calculated by,

$$f_{\text{Elastic}}(P_i, \sigma_{ij}) = -\frac{1}{2} s_{ijkl} \sigma_{ij} \sigma_{kl} - Q_{ijk} P_i P_j \sigma_{kl} \quad (3)$$

where s_{ijkl} , σ_{ij} , and Q_{ijk} were the elastic compliance tensor, stress tensor, and electrostrictive tensor measured experimentally. The electrostatic contribution could be calculated by,

$$f_{\text{Electric}}(P_i, E_i) = -\frac{1}{2} k_{ij}^b E_i E_j - E_i P_i \quad (4)$$

where E_i and k_{ij}^b were the applied electric field and background dielectric constant. Thus, the total free energy density could be described by,

$$G_{\text{Total}}(P_i, \sigma_{ij}, E_i) = f_{\text{Landau}} + f_{\text{Elastic}} + f_{\text{Electric}} \quad (5)$$

To describe the thermodynamic polydomain approximation, a similar approach to Koukhar et al. was taken.^[33] First, an inverse Legendre transform was applied to move from a Gibbs energy framework into a Helmholtz energy framework, that is, $\mathcal{F} = G + \sum_{n=1}^6 \sigma_n \varepsilon_n$, where the stress (σ_n) and strain (ε_n) were in Voigt notation, and the strain could be defined by $\varepsilon_n = -\frac{\partial G}{\partial \sigma_n}$. After proper manipulation the monodomain Helmholtz free energy could be described as a function of P_i and σ_n . Since only a periodic domain structure was considered, the minimization of the total free energy (\mathcal{F}) could be replaced by minimization of the mean energy density ($\bar{\mathcal{F}}$). This mean energy density could be calculated by

$$\langle \bar{\mathcal{F}} \rangle = \phi \bar{\mathcal{F}}' + (1 - \phi) \bar{\mathcal{F}}'' \quad (6)$$

where $\bar{\mathcal{F}}'$ and $\bar{\mathcal{F}}''$ were the monodomain free energy densities in the inner regions of the two domain types, where the polarization and strain/stress fields were uniform.

Using both mechanical and electrical boundary conditions, it was possible to eliminate the stresses (σ_i, σ_i') and internal electrical fields (E_i, E_i') from the mean energy density. For films grown on (001)-oriented cubic substrates, the in-plane size and shape of the film were controlled by a thick substrate, and thus imposed in-plane strains ($\langle u_1 \rangle, \langle u_2 \rangle, \langle u_6 \rangle$) on the film. This provided the following conditions,

$$\begin{aligned} \phi u_1' + (1 - \phi) u_1'' &= u_1 \\ \phi u_2' + (1 - \phi) u_2'' &= u_2 \\ \phi u_6' + (1 - \phi) u_6'' &= u_6 \end{aligned} \quad (7)$$

Here, it was assumed that $u_1 = u_2 = u_m$ and $u_6 = 0$. The isotropic misfit strain was calculated as $u_m = (b - a_0)/b$ where a_0 and b were the lattice parameters of the pseudocubic phase of the ferroelectric and the substrate, respectively. Similarly, the absence of traction forces on the surface of the film yielded the following boundary conditions

$$\phi \sigma_i' + (1 - \phi) \sigma_i'' = 0, \text{ where } i = 3, 4, 5 \quad (8)$$

Next, the so-called microscopic boundary conditions where the lattice strains must obey the classical compatibility condition were considered. Rotating the coordinate system (x_1^*, x_2^*, x_3^*) with the x_3^* axis orthogonal to the domain walls gave $u_i' = u_i''$ ($i = 1, 2, 6$) and $\sigma_i' = \sigma_i''$ ($i = 3, 4, 5$). The electrical continuity conditions yielded $E_i' = E_i''$ ($i = 1, 2$) and $\varepsilon_0 E_i' + P_i' = \varepsilon_0 E_i'' + P_i''$ ($i = 3$). Solving the boundary conditions and substituting into the mean free energy density, the mean energy density became a variable of seven variables (P_i', P_i'', ϕ , where $i = 1, 2, 3$). Performing numerical minimization, the equilibrium polarization and phase fractions could be determined as a function a temperature, misfit strain, and applied electric field. This approach required defined domain-wall orientations and, in this work, domain walls aligned along the (101) and (110), which was expected to occur in c/a and a_1/a_2 domain structures, respectively, were considered. The monodomain free energy was also computed. From these three different situations, the domain structure with the lowest energy was chosen as the stable phase and domain stability phase diagrams could be generated.

The relevant free energy coefficients and material constants used in the present calculations for the $\text{Pb}_{1-x}\text{Sr}_x\text{TiO}_3$ thin films were calculated as weighted averages of those for pure PbTiO_3 and SrTiO_3 except for α_1 .^[49] A so-called linearly averaged dielectric stiffness α_1 was chosen as was previously used in the literature,^[49] that is,

$$\alpha_1 = 5.65 \times 10^5 (T - 716.5x_{\text{Pb}} + 237.5) / (0.81 + 0.69x_{\text{Pb}}) \quad (9)$$

Here, T was temperature in $^\circ\text{C}$. The notation x_{Pb} denoted the mole fraction of lead in the solid solution $\text{Pb}_{1-x}\text{Sr}_x\text{TiO}_3$. Other material coefficients were $\alpha_{11} = -7.3 \times 10^7 x_{\text{Pb}} + 1.04 \times 10^8 (1 - x_{\text{Pb}})$, $\alpha_{12} = 7.5 \times 10^8 x_{\text{Pb}} + 7.46 \times 10^7 (1 - x_{\text{Pb}})$, $\alpha_{111} = 2.6 \times 10^8 x_{\text{Pb}}$, $\alpha_{112} = 6.1 \times 10^8 x_{\text{Pb}}$, $\alpha_{123} = -3.7 \times 10^9 x_{\text{Pb}}$, $Q_{11} = 0.089 x_{\text{Pb}} + 0.0496 (1 - x_{\text{Pb}})$, $Q_{12} = -0.026 x_{\text{Pb}} - 0.0131 (1 - x_{\text{Pb}})$, $Q_{44} = 0.0675 x_{\text{Pb}} + 0.019 (1 - x_{\text{Pb}})$, $S_{11} = 8.0 \times 10^{-12}$, $S_{12} = -2.5 \times 10^{-12}$, and $S_{44} = 9.0 \times 10^{-12}$.

Phase-Field Simulations: To simulate the polarization distribution and domain structure development in the single layer $\text{Pb}_{1-x}\text{Sr}_x\text{TiO}_3$ thin films, the phase-field method was utilized. The evolution of the polarization structure was governed by solving the time-dependent Ginzburg–Landau equation, that is,

$$\frac{\partial P_i(x,t)}{\partial t} = -L \frac{\delta F}{\delta P_i(x,t)} \quad (10)$$

Here, x , t , and L represent the spatial coordinate vector, time, and a kinetic coefficient relating to domain-wall motion. The total free energy functional (F) followed from above with the inclusion of a gradient energy contribution

$$F = \int_V (f_{\text{Landau}} + f_{\text{Elastic}} + f_{\text{Electric}} + f_{\text{Gradient}}) dV \quad (11)$$

The local gradient energy contribution could be defined as,

$$f_{\text{Gradient}} = \frac{1}{2} G_{ijkl} \frac{\partial P_i}{\partial x_j} \frac{\partial P_k}{\partial x_l} \quad (12)$$

where an isotropic gradient-energy tensor, G_{ijkl} , was assumed with renormalized values of $G_{11} = 1.0$, $G_{12} = -1.0$, and $G_{44} = 1.0$ in Voigt notation, whereas the elastic energy density in this case could be written as,

$$f_{\text{Elastic}} = c_{ijkl} (\epsilon_{ij} - \epsilon_{ij}^0) (\epsilon_{kl} - \epsilon_{kl}^0) \quad (13)$$

$$\epsilon_{ij}^0 = Q_{ijk} P_k P_l \quad (14)$$

where c_{ijkl} , Q_{ijk} , and ϵ_{ij} represented the stiffness tensor, electrostrictive tensor, and total strain, respectively. The electric energy density followed from the previous.

It was noted that in this work the background dielectric constants k_{ij}^0 were chosen as 20 and isotropic. No electric field was applied to the system (in either phase-field or thermodynamic calculations) and short-circuit boundary conditions were assumed. Information on solving the elastic and electrostatic equilibrium equations can be found in the literature.^[81] Last, the elastic and electrostatic equilibrium were presumed to occur instantaneously with respect to the polarization equilibrium.

A variety of system sizes were utilized to calculate the work presented herein with system sizes ranging from $(128\Delta x_1 \times 128\Delta x_2)$ to $(512\Delta x_1 \times 512\Delta x_2)$ in the lateral planar directions. A constant thickness of the film was used consisting of $20\Delta x_3$ grid points as the ferroelectric film, $12\Delta x_3$ grid points as the substrate, where the elastic constants were assumed to be the same as the film, and $4\Delta x_3$ grid points acting as a vacuum layer above the film. Periodic boundary conditions were applied for the in-plane lateral directions, whereas natural boundary conditions were applied to the film–vacuum and film–substrate interface. In all simulations $\Delta x_1 = \Delta x_2 = \Delta x_3 = 1$ nm. To initiate the simulation, a random noise was applied to each spatial vector point and the simulation was simulated to equilibrium (80 000 timesteps). The phase-field calculations were completed using the μPro software. Visualization of the domain structures were completed using a homegrown application using the Visualization Toolkit.

A variety of analysis techniques were utilized for post-processing the phase-field generated domain structures. To develop a binarized image, the elastic displacements of the film were summed through the thickness of the film, and then different domain regions were decided with the threshold value. Since the ferroelectric a_1/a_2 phase would be nearly flat from a topographical standpoint and the ferroelectric c/a phase would exhibit elastic displacement in the x_3 direction (parallel to the [001]), the summation of the elastic displacement allows for accurate determination of the c/a and a_1/a_2 domain locations and, therefore, their boundaries.

Pulsed-Laser Deposition of Thin-Film Heterostructures: All films were grown using pulsed-laser deposition in an on-axis geometry with a target-to-substrate distance of 60 mm, using a KrF excimer

laser (248 nm, LPX 300, Coherent). All films were grown from $\text{Pb}_{1.2}\text{TiO}_3$ ceramic target (K. J. Lesker) and SrTiO_3 single-crystal targets. The 20% excess lead in the $\text{Pb}_{1.2}\text{TiO}_3$ target was found to be vital to compensate the lead loss during the PbTiO_3 thin film growth. The growth rate was established for individual, single-layer PbTiO_3 and SrTiO_3 thin films grown on DyScO_3 (110) substrates (CrysTec GmbH) using X-ray reflectivity. The composition of the $\text{Pb}_{1-x}\text{Sr}_x\text{TiO}_3$ thin-film heterostructures was varied across $0 \leq x \leq 0.3$ using a sub-unit-cell-level mixing method from a $\text{Pb}_{1.2}\text{TiO}_3$ ceramic target (K. J. Lesker) and a SrTiO_3 single crystal target via a programmable target rotator (Neocera, LLC) that was synced in real-time with the excimer laser. For example, here, it took 60 pulses to grow a unit cell of PbTiO_3 and 50 pulses to grow a unit cell of SrTiO_3 . Therefore, a $\text{Pb}_{0.8}\text{Sr}_{0.2}\text{TiO}_3$ film could be achieved by growing a sequence of 24 pulses of PbTiO_3 , 5 pulses of SrTiO_3 , 24 pulses of PbTiO_3 , and 5 pulses of SrTiO_3 (for a total of 58 pulses; 48 from PbTiO_3 and 10 from SrTiO_3 making the right composition) overall. This approach was used in numerous prior works.^[20–22,82,83] The growth of the 100-nm-thick $\text{Pb}_{1-x}\text{Sr}_x\text{TiO}_3$ thin films ($0 \leq x \leq 0.3$) was completed on DyScO_3 (110) single-crystal substrates at a heater temperature of 640 °C, a dynamic oxygen pressure of 200 mTorr, a laser fluence of 1.8 J cm^{-2} , and the laser repetition rate was 10 and 2 Hz for growth of $\text{Pb}_{1.2}\text{TiO}_3$ and SrTiO_3 , respectively. The average uncertainty in the composition was $\approx 0.54\%$ as determined via X-ray diffraction analysis with respect to reference data.^[34] For dielectric measurements, additional top and bottom electrode contacts of SrRuO_3 were grown. The SrRuO_3 growth was carried out at a heater temperature of 640 °C in a dynamic oxygen pressure of 100 mTorr with a laser fluence of 1 J cm^{-2} and a laser repetition rate of 17 Hz from a ceramic target (Praxair) of the same composition. In all growths, the heterostructures were cooled from the growth temperature to room temperature at $10 \text{ }^\circ\text{C min}^{-1}$ in a static oxygen pressure of ≈ 760 Torr.

Determination of Crystal Structure via X-Ray Diffraction: The crystal structure of the synthesized $\text{Pb}_{1-x}\text{Sr}_x\text{TiO}_3$ films was determined using X-ray diffraction using a high-resolution X-ray diffractometer (Panalytical, X'Pert MRD) with fixed-incident-optics slits of $1/2^\circ$ for θ – 2θ and $1/32^\circ$ for RSM studies, copper K_α radiation (1.54 \AA), and a fixed receiving slit of 0.275 mm for the PIXcel3D-Medipix3 detector. θ – 2θ line scans were performed to investigate the domain structures in the direction perpendicular to the plane of the DyScO_3 (110) substrates. Additionally, to determine different crystal structure variants and domain tilts in the heterostructures, X-ray diffraction RSM studies were performed about the 220_0 -diffraction condition of the substrate.

Topography and Domain Structure Characterization: Topography study of the $\text{Pb}_{1-x}\text{Sr}_x\text{TiO}_3$ thin films was carried out using an AFM (MFP-3D, Asylum Research). All topography measurements were carried out using silicon AFM probe tips (Tap300Al-G BudgetSensor) with a force constant of 40 Nm^{-1} at a resonance frequency of $\approx 300 \text{ kHz}$ using the AC Air Topography mode (non-contact tapping mode).

Binarization of the AFM/Phase-Field Data: High-resolution AFM images ($512 \text{ points} \times 512 \text{ points}$) were used to study the phase distribution in each composition. First, each image was flattened with in-built functions (Planefit and masked flattening) of the Igor-pro-6.38B01 AFM image viewer to avert any artifacts coming from image capturing process and from any particles imaged during the AFM scan. The YellowHot256 color scheme was used to better distinguish different domain types. Other steps, like, removing legends, scales, and tick marks from the image, setting the range to 1 pm and offset value to zero were carried out before exporting the final image in .PNG format with the same resolution. The images were then processed via MATLAB using the imbinarize function to binarize the data with the white color assigned to the c/a domains and the black color assigned to the a_1/a_2 domains.

Euler Characteristic Analysis: Fully binarized images were then processed with the bwlabel function available within the Image Processing Toolbox of MATLAB to calculate the EC (χ). To compute the normalized EC (χ_N), the required total number of connected objects in the image was determined using the bwconncomp function available within the Image Processing Toolbox of MATLAB.

Area Fraction and Perimeter Calculation: The area of the c/a domain was calculated using the sum function available with arithmetic operation functions of MATLAB on the matrix representing binarized image. A detailed procedure to obtain such binarized images from the AFM topography scans was explained in the “Binarization of the AFM/Phase-Field Data” section. This area was then normalized with the total area of the image to calculate the c/a domain fraction. The same image was then used to calculate the shared perimeter by using the bwperim function available within the Image Processing Toolbox of MATLAB.

Annealing Procedure: Samples were annealed, in air, on a hot plate for times ranging from 12 to 190 h with the temperature set to 270 °C. An effective heating and cooling rate of 5 °C min⁻¹ was maintained during heating and cooling. The samples were mounted on glass slides using silver paint for proper thermal contact and to aid in transporting the sample between measurements. After each annealing cycle, AFM topography was checked to record the domain structures. Multiple heating cycles were done on specific samples to reach (cumulative) total anneal times.

Electrical and Dielectric Characterization: The electrical properties for all the $\text{Pb}_{1-x}\text{Sr}_x\text{TiO}_3$ ($0 < x < 0.3$) heterostructures were studied with symmetric 30 nm-thick SrRuO_3 films serving as the top and bottom electrodes. The measurements were performed with circular capacitor (diameter of 25 μm) structures patterned on the top electrode via wet chemical etching via 0.1 M NaIO_4 solution. The polarization as a function of electric field (–400 to 400 kV cm⁻¹) for these circular capacitor structures was measured using a Precision Multiferroic Tester (Radiant Technologies, Inc.) at room temperature. Dielectric and loss tangent measurements were performed using an E4990A Impedance Analyzer (Keysight Technologies) at room temperature and frequency (1–1000 kHz) up to an AC field strength value of 400 kV cm⁻¹. Background DC bias (0 to –200 kV cm⁻¹) was applied to study the intrinsic and intrinsic-extrinsic combined contribution of dielectric permittivity intercept at zero field.

Supporting Information

Supporting Information is available from the Wiley Online Library or from the author.

Acknowledgements

P.K. and J.A.Z. contributed equally to this work. P.K. acknowledges support from the Army Research Office via Grant W911NF-21-1-0118. J.A.Z. acknowledges the support of 3M Incorporated for their support via a fellowship. A.D. acknowledges support from the Army Research Office via Grant W911NF-21-1-0126. J.A.Z., B.W., L.-Q.C., and L.W.M. acknowledge support from the Army Research Office under the ETHOS MURI via cooperative agreement W911NF-21-2-0162. M.R. acknowledges support from the Intel Corp. under the COFEE program. Computations for this research were performed on the Pennsylvania State University’s Institute for Cyber and Data Science Advanced CyberInfrastructure (ICDS-ACI). This work used the Extreme Science and Engineering Discovery Environment (XSEDE), which is supported by National Science Foundation grant number ACI-1548562. Specifically, it used the Bridges system, which is supported by NSF award number ACI-1445606, at the Pittsburgh Supercomputing Center (PSC). The authors acknowledge the Texas Advanced Computing Center (TACC) at The University of Texas at Austin for providing HPC resources that have contributed to the research results reported within this paper.

Conflict of Interest

The authors declare no conflict of interest.

Data Availability Statement

Research data are not shared.

Keywords

domains, Euler characteristics, ferroelectric thin films, mixed-phase domain structures, topology

Received: April 17, 2022

Revised: July 8, 2022

Published online: August 15, 2022

- [1] T. Nagaya, J. M. Gilli, *Phys. Rev. E: Stat. Phys., Plasmas, Fluids, Relat. Interdiscip. Top.* **2002**, 65, 8.
- [2] A. Sehgal, V. Ferreiro, J. F. Douglas, E. J. Amis, A. Karim, *Langmuir* **2002**, 18, 7041.
- [3] G. Nisato, B. D. Ermi, J. F. Douglas, A. Karim, *Macromolecules* **1999**, 32, 2356.
- [4] A. Stein, G. Wright, K. G. Yager, G. S. Doerk, C. T. Black, *Nat. Commun.* **2016**, 7, 12366.
- [5] L. Sánchez-Munõz, A. Del Campo, J. F. Fernández, *Sci. Rep.* **2016**, 6, 20806.
- [6] T. Garel, S. Doniach, *Phys. Rev. B* **1982**, 26, 325.
- [7] R. P. Huebener, *Magnetic Flux Structures in Superconductors*, Springer-Verlag, Berlin, Germany **2001**.
- [8] A. D. D. Craik, *Fluid Dyn. Res.* **2000**, 26, 305.
- [9] X. Yu, M. Mostovoy, Y. Tokunaga, W. Zhang, K. Kimoto, Y. Matsui, Y. Kaneko, *Proc. Natl. Acad. Sci. USA* **2017**, 114, E265.
- [10] A. K. Yadav, C. T. Nelson, S. L. Hsu, Z. Hong, J. D. Clarkson, C. M. Schlepütz, A. R. Damodaran, P. Shafer, E. Arenholz, L. R. Dedon, D. Chen, A. Vishwanath, A. M. Minor, L. Q. Chen, J. F. Scott, L. W. Martin, R. Ramesh, *Nature* **2016**, 530, 198.
- [11] S. Das, Y. L. Tang, Z. Hong, M. A. P. Gonçalves, M. R. McCarter, C. Klewe, K. X. Nguyen, F. Gómez-Ortiz, P. Shafer, E. Arenholz, V. A. Stoica, S. L. Hsu, B. Wang, C. Ophus, J. F. Liu, C. T. Nelson, S. Saremi, B. Prasad, A. B. Mei, D. G. Schlom, J. Íñiguez, P. García-Fernández, D. A. Muller, L. Q. Chen, J. Junquera, L. W. Martin, R. Ramesh, *Nature* **2019**, 568, 368.
- [12] Y. J. Wang, Y. P. Feng, Y. L. Zhu, Y. L. Tang, L. X. Yang, M. J. Zou, W. R. Geng, M. J. Han, X. W. Guo, B. Wu, X. L. Ma, *Nat. Mater.* **2020**, 19, 881.
- [13] W. Pompe, X. Gong, Z. Suo, J. S. Speck, *J. Appl. Phys.* **1993**, 74, 6012.
- [14] R. Uecker, D. Klimm, R. Bertram, M. Bernhagen, I. Schulze-Jonack, M. Brützmam, A. Kwasniewski, T. M. Gesing, D. G. Schlom, *Acta Phys. Pol. A* **2013**, 124, 295.
- [15] N. A. Pertsev, A. G. Zembilgotov, *J. Appl. Phys.* **1995**, 78, 6170.
- [16] A. R. Damodaran, S. Pandya, J. C. Agar, Y. Cao, R. K. Vasudevan, R. Xu, S. Saremi, Q. Li, J. Kim, M. R. McCarter, L. R. Dedon, T. Angsten, N. Balke, S. Jesse, M. Asta, S. V. Kalinin, L. W. Martin, *Adv. Mater.* **2017**, 29, 1702069.
- [17] X. Lu, Z. Chen, Y. Cao, Y. Tang, R. Xu, S. Saremi, Z. Zhang, L. You, Y. Dong, S. Das, H. Zhang, L. Zheng, H. Wu, W. Lv, G. Xie, X. Liu, J. Li, L. Chen, L. Q. Chen, W. Cao, L. W. Martin, *Nat. Commun.* **2019**, 10, 3951.
- [18] A. R. Damodaran, J. D. Clarkson, Z. Hong, H. Liu, A. K. Yadav, C. T. Nelson, S. L. Hsu, M. R. McCarter, K. D. Park, V. Kravtsov, A. Farhan, Y. Dong, Z. Cai, H. Zhou, P. Aguado-Puente, P. Garcia-Fernandez, J. Iniguez, J. Junquera, A. Scholl, M. B. Raschke, L. Q. Chen, D. D. Fong, R. Ramesh, L. W. Martin, *Nat. Mater.* **2017**, 16, 1003.

- [19] J. Zhuang, A. A. Bokov, N. Zhang, J. Zhang, J. Zhao, S. Yang, W. Ren, Z. G. Ye, *Cryst. Growth Des.* **2018**, *18*, 4503.
- [20] J. C. Agar, A. R. Damodaran, M. B. Okatan, J. Kacher, C. Gammer, R. K. Vasudevan, S. Pandya, L. R. Dedon, R. V. K. Mangalam, G. A. Velarde, S. Jesse, N. Balke, A. M. Minor, S. V. Kalinin, L. W. Martin, *Nat. Mater.* **2016**, *15*, 549.
- [21] R. V. K. Mangalam, J. Karthik, A. R. Damodaran, J. C. Agar, L. W. Martin, *Adv. Mater.* **2013**, *25*, 1761.
- [22] A. R. Damodaran, S. Pandya, Y. Qi, S. L. Hsu, S. Liu, C. Nelson, A. Dasgupta, P. Ercius, C. Ophus, L. R. Dedon, J. C. Agar, H. Lu, J. Zhang, M. Andrew, A. M. Rappe, L. W. Martin, *Nat. Commun.* **2017**, *8*, 14961.
- [23] G. Velarde, S. Pandya, L. Zhang, D. Garcia, E. Lupi, R. Gao, J. D. Wilbur, C. Dames, L. W. Martin, *ACS Appl. Mater. Interfaces* **2019**, *11*, 35146.
- [24] J. E. McClure, T. Ramstad, Z. Li, R. T. Armstrong, S. Berg, *Transp. Porous Media* **2020**, *133*, 229.
- [25] H. Jinai, T. Kajihara, H. Watashiba, Y. Nishikawa, R. J. Spontak, *Phys. Rev. E: Stat. Phys., Plasmas, Fluids, Relat. Interdiscip. Top.* **2001**, *64*, 010803.
- [26] Y. Nahas, S. Prokhorenko, Q. Zhang, V. Govinden, N. Valanoor, L. Bellaiche, *Nat. Commun.* **2020**, *11*, 5779.
- [27] Y. Nahas, S. Prokhorenko, J. Fischer, B. Xu, C. Carrétero, S. Prosandeev, M. Bibes, S. Fusil, B. Dkhil, V. Garcia, L. Bellaiche, *Nature* **2020**, *577*, 47.
- [28] Q. Zhang, L. Xie, G. Liu, S. Prokhorenko, Y. Nahas, X. Pan, L. Bellaiche, A. Gruverman, N. Valanoor, *Adv. Mater.* **2017**, *29*, 1702375.
- [29] Q. Zhang, S. Prokhorenko, Y. Nahas, L. Xie, L. Bellaiche, A. Gruverman, N. Valanoor, *Adv. Funct. Mater.* **2019**, *29*, 1808573.
- [30] V. Govinden, S. Rijal, Q. Zhang, D. Sando, S. Prokhorenko, Y. Nahas, L. Bellaiche, N. Valanoor, *Phys. Rev. Mater.* **2021**, *5*, 124205.
- [31] M. Seul, D. Andelman, *Science* **1995**, *267*, 476.
- [32] A. J. Bray, *Adv. Phys.* **1994**, *43*, 357.
- [33] R. Waser, N. A. Pertsev, V. G. Koukhar, *Phys. Rev. B: Condens. Matter Mater. Phys.* **2001**, *64*, 214103.
- [34] G. Rispiens, J. A. Heuver, B. Noheda, *Appl. Phys. Lett.* **2010**, *97*, 262901.
- [35] G. Catalan, A. Janssens, G. Rispiens, S. Csiszar, O. Seeck, G. Rijnders, D. H. A. Blank, B. Noheda, *Phys. Rev. Lett.* **2006**, *96*, 127602.
- [36] S. Pandya, J. Wilbur, J. Kim, R. Gao, A. Dasgupta, C. Dames, L. W. Martin, *Nat. Mater.* **2018**, *17*, 432.
- [37] J. L. Jones, E. B. Slamovich, K. J. Bowman, *J. Appl. Phys.* **2005**, *97*, 034113.
- [38] Y. Ehara, S. Yasui, T. Oikawa, T. Shiraishi, T. Shimizu, H. Tanaka, N. Kanenko, R. Maran, T. Yamada, Y. Imai, O. Sakata, N. Valanoor, H. Funakubo, *Sci. Rep.* **2017**, *7*, 9641.
- [39] G. Peng, F. Qiu, V. V. Ginzburg, D. Jasnow, A. C. Balazs, *Science* **2000**, *288*, 1802.
- [40] R. Shimizu, H. Tanaka, *Sci. Adv.* **2017**, *3*, eaap9570.
- [41] F. S. Bates, G. H. Fredrickson, *Phys. Today* **1999**, *52*, 32.
- [42] E. Richardson, M. Werman, *Pattern Recognit. Lett.* **2014**, *49*, 99.
- [43] E. Amorim, R. A. Moreira, F. A. N. Santos, *bioRxiv* **2019**, <https://doi.org/10.1101/871632>.
- [44] A. Smith, V. M. Zavala, *Comput. Chem. Eng.* **2021**, *154*, 107463.
- [45] L. Euler, *Novi Comment. Acad. Sci. Petropol.* **1758**, *4*, 109.
- [46] K. Scholz, F. Wirner, J. Götz, U. Råde, G. E. Schröder-Turk, K. Mecke, C. Bechinger, *Phys. Rev. Lett.* **2012**, *109*, 264504.
- [47] H.-J. Vogel, in *Morphology of Condensed Matter* (Eds: K. Mecke, D. Stoyan), Springer, Berlin, Germany **2002**, p. 75.
- [48] G. L. X. Xing, J. Chen, J. Deng, *J. Alloys Compd.* **2003**, *360*, 286.
- [49] Y. Ding, W. Ma, *AIP Adv.* **2020**, *10*, 015022.
- [50] M. Jain, S. B. Majumder, R. Guo, A. S. Bhalla, R. S. Katiyar, *Mater. Lett.* **2002**, *56*, 692.
- [51] D. H. Kang, J. H. Kim, J. H. Park, K. H. Yoon, *Mater. Res. Bull.* **2001**, *36*, 265.
- [52] S. H. Leal, M. T. Escote, F. M. Pontes, E. R. Leite, M. R. Joya, P. S. Pizani, E. Longo, J. A. Varela, *J. Alloys Compd.* **2009**, *475*, 940.
- [53] F. A. N. Santos, M. D. Coutinho-Filho, *Phys. Rev. E: Stat., Nonlinear, Soft Matter Phys.* **2009**, *80*, 031123.
- [54] M. Pettini, *Geometry and Topology in Hamiltonian Dynamics and Statistical Mechanics, Interdisciplinary Applied Mathematics*, vol. 33, Springer, New York **2007**, p. 1.
- [55] P. Blanchard, D. Gandolfo, S. Shlosman, J. Ruiz, *Markov Processes Relat. Fields* **2003**, *9*, 523.
- [56] P. Blanchard, S. Fortunato, D. Gandolfo, *Nucl. Phys. B* **2002**, *644*, 495.
- [57] J. A. Rehn, F. A. N. Santos, M. D. Coutinho-Filho, *Braz. J. Phys.* **2012**, *42*, 410.
- [58] P. Blanchard, C. Dobrovolny, D. Gandolfo, J. Ruiz, *J. Stat. Mech.: Theory Exp.* **2006**, *2006*, P03011.
- [59] D. Gandolfo, *Phys. A* **2005**, *358*, 22.
- [60] F. A. N. Santos, E. P. Raposo, M. D. Coutinho-Filho, M. Copelli, C. J. Stam, L. Douw, *Phys. Rev. E* **2019**, *100*, 032414.
- [61] N. Linial, Y. Peled, *Ann. Math.* **2016**, *184*, 745.
- [62] T. Shimada, Y. Wang, T. Hamaguchi, K. Kasai, K. Masuda, L. Van Lich, T. Xu, J. Wang, H. Hirakata, *J. Phys.: Condens. Matter* **2021**, *33*, 505301.
- [63] L. Van Lich, Q. T. Ton, T. G. Nguyen, V. H. Dinh, *Appl. Phys. Lett.* **2019**, *114*, 022901.
- [64] K. E. Kim, S. Jeong, K. Chu, J. H. Lee, G. Y. Kim, F. Xue, T. Y. Koo, L. Q. Chen, S. Y. Choi, R. Ramesh, C. H. Yang, *Nat. Commun.* **2018**, *9*, 403.
- [65] N. Schupper, N. M. Shnerb, *Phys. Rev. E* **2005**, *72*, 046107.
- [66] O. Portmann, A. Vaterlaus, D. Pescia, *Nature* **2003**, *422*, 701.
- [67] S. Echeverría-Alar, M. G. Clerc, *Phys. Rev. Res.* **2020**, *2*, 042036.
- [68] F. Ritort, P. Sollich, *Adv. Phys.* **2003**, *52*, 219.
- [69] K. U. Deniz, *Bull. Mater. Sci.* **1988**, *10*, 61.
- [70] T. Passot, A. C. Newell, *Phys. D* **1994**, *74*, 301.
- [71] A. O. Leonov, U. K. Rößler, M. Mostovoy, *EPJ Web Conf.* **2014**, *75*, 14.
- [72] A. C. Newell, T. Passot, N. Ercolani, R. Indik, *J. Phys. II* **1995**, *5*, 1863.
- [73] S. Matzen, S. Fusil, *C. R. Phys.* **2015**, *16*, 227.
- [74] G. F. Nataf, M. Guennou, J. M. Gregg, D. Meier, J. Hlinka, E. K. H. Salje, J. Kreisel, *Nat. Rev. Phys.* **2020**, *2*, 634.
- [75] R. Xu, J. Karthik, A. R. Damodaran, L. W. Martin, *Nat. Commun.* **2014**, *5*, 3120.
- [76] J. Karthik, A. R. Damodaran, L. W. Martin, *Phys. Rev. Lett.* **2012**, *108*, 167601.
- [77] A. R. Damodaran, C. W. Liang, Q. He, C. Y. Peng, L. Chang, Y. H. Chu, L. W. Martin, *Adv. Mater.* **2011**, *23*, 3170.
- [78] S. Pandya, G. A. Velarde, R. Gao, A. S. Everhardt, J. D. Wilbur, R. Xu, J. T. Maher, J. C. Agar, C. Dames, L. W. Martin, *Adv. Mater.* **2019**, *31*, 1803312.
- [79] Z. Li, M. Grimsditch, X. Xu, S. K. Chan, *Ferroelectrics* **1993**, *141*, 313.
- [80] M. Narayanan, S. Tong, S. Liu, B. Ma, U. Balachandran, *Appl. Phys. Lett.* **2013**, *102*, 062906.
- [81] Y. L. Li, S. Y. Hu, Z. K. Liu, L. Q. Chen, *Appl. Phys. Lett.* **2002**, *81*, 427.
- [82] M. Acharya, E. Banyas, M. Ramesh, Y. Jiang, A. Fernandez, A. Dasgupta, H. Ling, B. Hanrahan, K. Persson, J. B. Neaton, L. W. Martin, *Adv. Mater.* **2022**, *34*, 2105967.
- [83] R. V. K. Mangalam, J. C. Agar, A. R. Damodaran, J. Karthik, L. W. Martin, *ACS Appl. Mater. Interfaces* **2013**, *5*, 13235.